Kuwait J.Sci., Vol.50, No.(3A),July.2023,pp(1-14)

Magnetic properties of Ba Ferrite Substituted by Low Fraction of Ni Cations

Luma H. Abdel-Mohsen[1] , Sadeq H.Lafta[2,*], Mustafah Sh.Hashim[3]

[1, 3] *Physics department, Education College, Mustansiriya University, Baghdad, Iraq.*
[2]*Applied Science Department, University of Technology-Iraq, Baghdad, Iraq.*

**Corresponding author: Sadeq.h.lafts@uotechnology.edu.iq*

Abstract

Four compositions of spinel $Ni_xBa_{1-x}Fe_2O_4$ of x =0, 0.05, 0.01, and 0.15 were prepared by the auto-combustion route. X-ray diffraction (XRD), Fourier transform infrared spectroscopy (FTIR), and Scanning Electron Microscopy (SEM) analyses were utilized to determine the structural properties. All samples showed a cubic spinel structure with a noticeable FTIR tetrahedral band blue shift as the molar ratio x was increased. The crystallite size and particle size have the same behavior as x changed from 0 to 0.15. Spherical nanoparticles aggregated into large clusters were found throughout the samples. Magnetic properties, displayed a drop in magnetization saturation as x increased to its max value. A saturation magnetization (M_s) of more than 48 emu/g was achieved at x = 0 and x = 0.15 while the coercivity did not change clearly. The fitting by the Langevin equation using Originlab software showed very close values of Ms to those measured by the vibrating sample magnetometer (VSM) test. Magnetic parameters are generally affected by both composition and particle size.

Keywords: Ba ferrite; langevin fitting ; magnetic properties; spinel; structural properties**.**

1. Introduction

Cubic spinel ferrite in nano-size has great significance because of its unique properties. Spinel ferrite possesses the prompt $M^{2+}Fe_2O_4$ where M is a binary valence cation with 8 formula /unit cell (Mulyawan *et al*, 2017). The octahedral sites contain 32 B-sites, and 64 A-sites for the tetrahedral sites (Saba *et al*, 2021). M-type Barium ferrite has a hexagonal structure and owns the prompt $BaFe_{12}O_{19}$ (Khotib *et al*, 2019). Ferrites have a huge resistivity, a trivial eddy current and low magnetic losses, relatively low cost, good chemical stability (Muhammad *et al*, 2018; Bogdan *et al* 2017), superparamagnetism state, magnetic tunneling, good biocompatibility and easy to be synthesized (Rohit *et al*, 2019).

Ferrites are divided into soft and hard. This classification makes ferrite to be suitable for large applications like electronics and microwave devices (Mulyawan *et al*, 2017), recording media, biomedicine, water purification (Rohit *et al*, 2019), drug delivery, hyperthermia, pigments, magnetic resonance imaging, Li-ion batteries electrodes and supercapacitors (Swati *et al*, 2018).

Synthesizing method has an essential role in crystallizing and particle size controlling. The auto-combustion technique owns a low cost and produces small changes in particle size. Different fuels were used in this process. The heavily used one is the Citric acid (Ravleen *et al*, 2020).

(Sachin *et al*, 2021) synthesized $BaFe_{12}O_{19}$ via auto combustion process utilizing Jamun pulp as a fuel with different concentrations and firing at 900°C. The saturation magnetization (M_s) was 58.9emu/g. (Yassine *et al*, 2020) prepared $Sr_{0.5}Ba_{0.5}Tm_xSm_xFe_{12-2x}O_{19}$ (x = 0.00–0.05) by the combustion technique with an M_s value in the range of 48.1–64.6 emu/g. (Tahseen *et al*, 2017) used the auto combustion method to synthesize ($BaFe_{12}O_{19}$) and fired it in the range of 700-900°C. The particle sizes of their samples were (0.5, 0.6 and 0.8 μm). (Widyastuti *et al*, 2017) synthesized ($BaFe_{12}O_{19}$) using the auto combustion method. Ni and Zn were used as substitutions with mole fractions of 0.2, 0.4, and 0.6. The firing was at (600°C). The Ms of their samples was 95.48emu/g.

In this study, an unprecedented Ba ferrite with a spinel structure was prepared and substituted with low nickel content. The study is supported by structural and magnetic analyses. A fitting was conducted to check some magnetic parameters.

2. Experimental

The used precursors were $Ni(NO_3)_2$, $Ba(NO_3)_2$, $Fe(NO_3)_3$, NH_4OH and citric acid provided by Central Drug House. The metal salts were weighted as in Table1 and dissolved in 200 ml of distilled water in a beaker. A homogeneous aqueous solution was obtained by intensive stirring. The molar ratio of citric acid:iron nitrate was fixed at 1:1. Then, NH_4OH was added until pH=7.5. Then the solution was heated to 80 °C to obtain the powder, followed by washing the powder with distilled water and methanol centrifugally, followed by firing at 600 °C for two hours.

Table 1. The weights of the used salts for preparation of Ba ferrite.

Sample	Molar ratio (x)	$(Fe(NO_3)_3.9H_2O)$ (g)	$Ni(NO_3)_2$ (g)	$(Ba(No_3)_2)$ (g)	$(C_6H_8O_7.H_2O)$ (g)	NH_4OH
1	0.0	11.627	0.00	0.654	6.00	Till=7.5
2	0.05	12.12	0.0365	0.627	6.00	Till=7.5
3	0.1	12.1243	0.0725	0.5883	5.7615	Till=7.5
4	0.15	12.12	0.109	0.55	6.00	Till=7.5

The analysis devices were XRD Shimadzu 6000 x-ray diffractometer, SEM MIRA3 TESCAN, FTIR device was Spectrum Two N PerkinElmer Inc. and VSM device was MDK.

3. Results and Discussion

3.1. The XRD Analysis

Figure 1 displays the XRD patterns of the fired and non-fired samples at different Ni molar ratios. There is no large difference between the fired and non-fired patterns. The important note for the

firing action is the rising of the peak around 33° which is related to, as expected, hematite formation (Sadeq 2017). The whole pattern shows a predominant cubic spinel structure. The XRD peaks (Miller indices) that match the spinel structure are (202), (311), (222), (400), (313), (422), (333), (404), (531), (424), (602), (533), (622) and (444), which correspond to the 2Θ around 30.33˚, 35.74˚, 37.38˚, 43.40˚, 47.55˚, 53.80˚, 57.45˚, 63.08˚, 66.50˚, 67.26˚, 71.67˚, 74.74˚, 75.73˚ and 79.67˚ in fit matching with magnetite JCPDF card no.96-900-2321 .

One can specify that all the synthesized samples belong to the cubic spinel phase of space group Fd3m. MFe_2O_4 can take different structures, which are spinel (normal and inverse), post spinel, and stuffed tridimite rhombohedral (Yuichi *et al*, 2020). Another study (Ch.Sarda *et al*, 1992) suggested residing Ba cations at the surface of γ-Fe_2O_3 and α-Fe_2O_3 submicron particles depending on the fact that large ions, like Ba (0.142 nm), may not be within such a cubic structure. The comparison between these study samples and the results of the latter mentioned studies gives reason to believe that the synthesized phase is spinel ferrite. The patterns of all samples match the cubic spinel structure of JCPDF card no.46-0113 very well.(B. C. Brightlin *et al,* 2016). The stuffed rhombohedral structure, (PDF: 00-020-0130), and post spinel of the orthorhombic structure with JCPDS card no.46-0113 (HANANE FODIL *et al*, 2017) have different patterns, hence they are excluded.

On the other hand, the probability of forming $BaCO_3$ of JCPDS No. 05-0378 and γ- Fe_2O_3 of JCPDS card No. 39-1346, as given in (Mali *et al*, 2005), despite the similarity of the diffraction peaks, is eliminated. This is because of the low intensity of the peak at 23.9˚ of the $BaCO_3$, which means forming a low quantity of $BaCO_3$. Besides, Ba^{2+} content measured by EDX, as it will be shown in section 3.4, is too much to be considered only residing on particle surfaces. The Ba content in the washing water is so small (less than 0.01wt% of the sample), as the atomic absorption analysis showed, which means most Ba atoms are involved in the synthesized solid structure. The last disagreement with the formation of the spinel structure is that Ba^{2+} has a large ionic radius that prevents it from being present in the spinel structure. Here, it is good to mention that the measured lattice constant was no less than 0.829 which does not contrast with a large radius of Ba^{2+} (0.142 nm). The upper explanation was given to compare this study's results with other studies supported with evidence to prove the formation of spinel structure. There are different studies that point to spinel $BaFe_2O_4$ formation (Sachin *et al*, 2021; Yue Liu, 2011) with no evidence of the existence of such a structure. These analyses support the formation of spinel Ba ferrite and no other spinel phase.

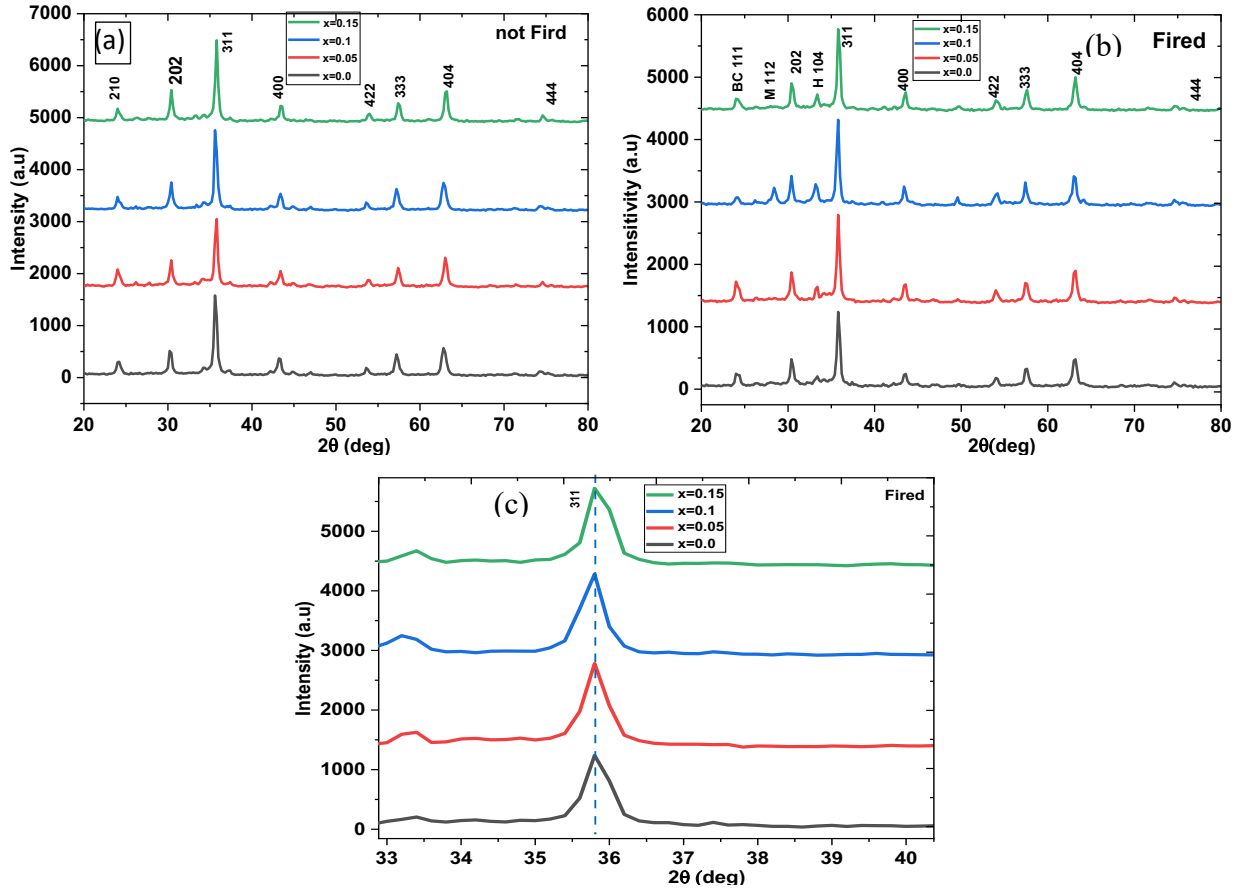

Fig. 1. XRD patterns of the prepared samples. (a) Samples that were not fired, (b) Samples that were fired at 600 C, and (c) Sample peaks at 2=35.74 with Miller indecies (311).Peakes were assigned H for hematite, BC for barium carbonate, M for maghemite and no sign for spinel ferrite.

The peaks cited at 2Θ of 24.27˚, 33.8˚, 42.8˚ and 44.9˚ don't match the spinel pattern, so they belong to other phases having a small amount, because their intensities are low compared to the spinel peaks. Hematite has peaks at, 33.8, 35.93, 62.97, and 24.33, which may relate to the mismatched peaks. Figure (1)c represents an enlargement of the peak for hkl (311), which shows that all peaks have the same 2Θ value, i.e. no shifts in the 2Θ values as a result of substitution were made.

The lattice constant "a" is calculated by (Saba *et al*, 2021):

$$a_{exp} = d_{hkl}\,(h^2 + k^2 + l^2)^{\frac{1}{2}} \quad \ldots \quad (1)$$

Where d_{hkl} is the interplane spacing. The X-ray density ρ_{XRD} is (Wei *et al*, 2019):

$$\rho_{XRD} = 8\frac{M}{N_A}a^3 \quad \ldots \quad (2)$$

The average crystallite size (L) is given by (Reem *et al*, 2022):

$$L = 0.9\,\lambda / \beta cos\theta \quad \ldots \quad (3)$$

The ionic radii of A-site and B-site (r_A, r_B), and bond lengths of tetrahedral (A-O) and octahedral (B-O) sites are given by (Muhammad *et al*, 2018):

$$r_A = (\mu - \tfrac{1}{4})a\sqrt{3} - r_o \quad \ldots \quad (4)$$

$$r_B = \left(\tfrac{5}{8} - \mu\right)a - r_o \quad \ldots \quad (5)$$

$$A - O = (\mu - \tfrac{1}{4})a\sqrt{3} \quad \ldots \quad (6)$$

$$B - O = (\tfrac{5}{8} - \mu)a \quad \ldots \quad (7)$$

Where r_O is the oxygen ion radius (1.35 Å); μ for spinel equals 3/8. The results are listed in Table 2. The tetrahedral and octahedral hopping lengths are denoted by (h_A) and the (h_B), and given by equations (8) and (9) (Wei *et al*, 2019) and listed also in Table 2.

$$h_A = a\,(3^{1/2}/4) \quad \ldots \quad (8)$$

$$h_B = a\,(2^{1/2}/4) \quad \ldots \quad (9)$$

Table 2. The XRD parameters at different molar ratio (x).

Parameter	x=0.0	x=0.05	x=0.1	x=0.15
a (nm)	0.830	0.830	0.8313	0.8292
ρ_{XRD} (g/cm^3)	7.280	7.173	7.057	7.020
L (nm)	28.01	18.67	17.50	24.01
Dislocation density x10^{-3} 1/L^2 (nm^{-2})	1.274	2.868	3.265	1.734
r_A (nm)	0.0446	0.0448	0.0450	0.0445
r_B (nm)	0.0724	0.0726	0.0728	0.0723
A-O (nm)	0.1796	0.1798	0.18	0.1795
B-O (nm)	0.2074	0.2076	0.209	0.2073
h_A (nm)	0.3593	0.3595	0.36	0.359
h_B (nm)	0.2933	0.2936	0.294	0.2932

The a parameter generally increases slightly as x increases. It is believed that the substitution action is sensible at the molar ratio of x = 0, where a noticeable growth occurs due to the substitution of some Ba^{2+} by a lower cation size Ni^{2+}. The reduction in the ρ_{XRD} is for the same later reason. The behavior of (L) shows a drop and then increases as (x) increases due to the increasing nucleation rate and increasing nucleation centers (Sadeq, 2020).

When x = 0.1, the crystallite size increases as the nucleation rate reaches saturation. A-site and B-site, A-O and B-O, and A-site and B-site are all dependent on the lattice constant, so they follow its behavior.

3.2. The FTIR Analysis

Figure 2(a) shows the infrared transmittance spectra of the samples, where all the spectra indicate the characteristic bands at 550-600 cm^{-1} of the stretching vibrations and 400-450 cm^{-1} of the lattice vibrations for the tetrahedral and octahedral sites, respectively (Zehra *et al*, 2014; Badawi *et al*, 2020). The former vibration band (555.4 cm^{-1}) is because of the metal-oxygen (Fe^{3+}-O^{2-}) stretching (Y. K. Dasan *et al*, 2017), it may shift depending on bond type and length (Raghvendra *et al*, 2018; Srinivasan *et al*, 1984).

The presence of different cations, such as Ba^{2+}, Fe^{3+}, and Ni^{2+}, may cause the splitting of the tetrahedral absorption band, as shown in Figure 2(b) (Shokrollahi *et al*., 2016). Further, the spectra show absorption bands at 1638.32 cm-1 corresponding to $NO3^{-1}$ ions and the (COO^{-}) group (Dasan *et al*. 2017). The weak absorption bands at 2975cm^{-1} are due to O-H stretching of H_2O (Anand *et al*, 2019; Badawi *et al*, 2020; Sachin *et al*, 2021). There is a shift in the octahedral band to higher values as seen in Figure (2)b because of substitution in the tetrahedral and octahedral sites by Ni^{2+}.

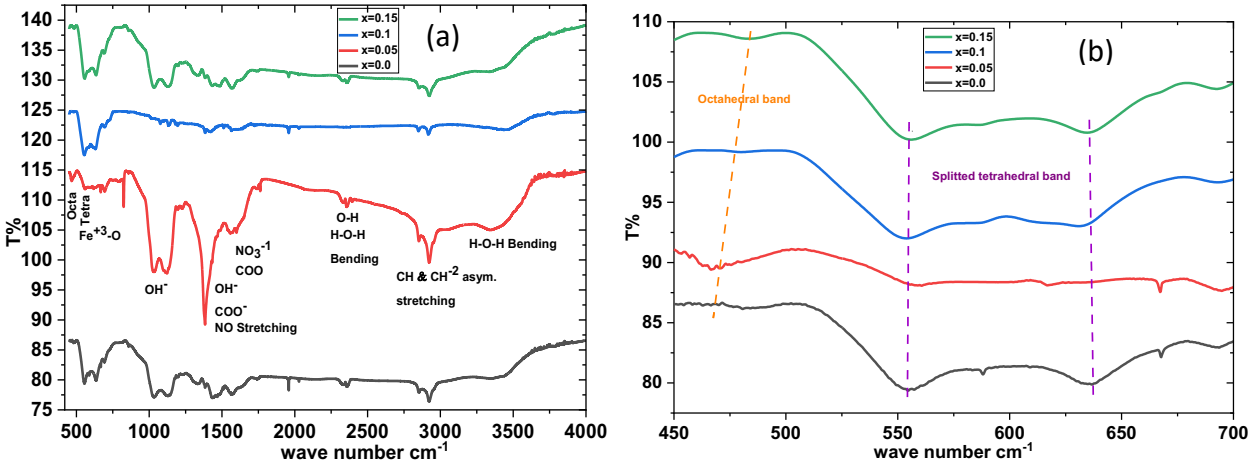

Fig. 2. The FTIR spectra of the samples. (a) FTIR spectrum 400–4000 cm-1 and (b) 450–700 cm^{-1} magnification showing octahedral and tetrahedral vibration modes.

3.3. Morphology Analysis

Figure 3(a) illustrates the SEM images of the samples and their particle distributions. As shown, the particles have homogenous size distributions. All $Ni_xBa_{1-x}Fe_2O_4$ samples revealed a granular structure consisting mainly of spherical grains with a norma distribution of particle size.

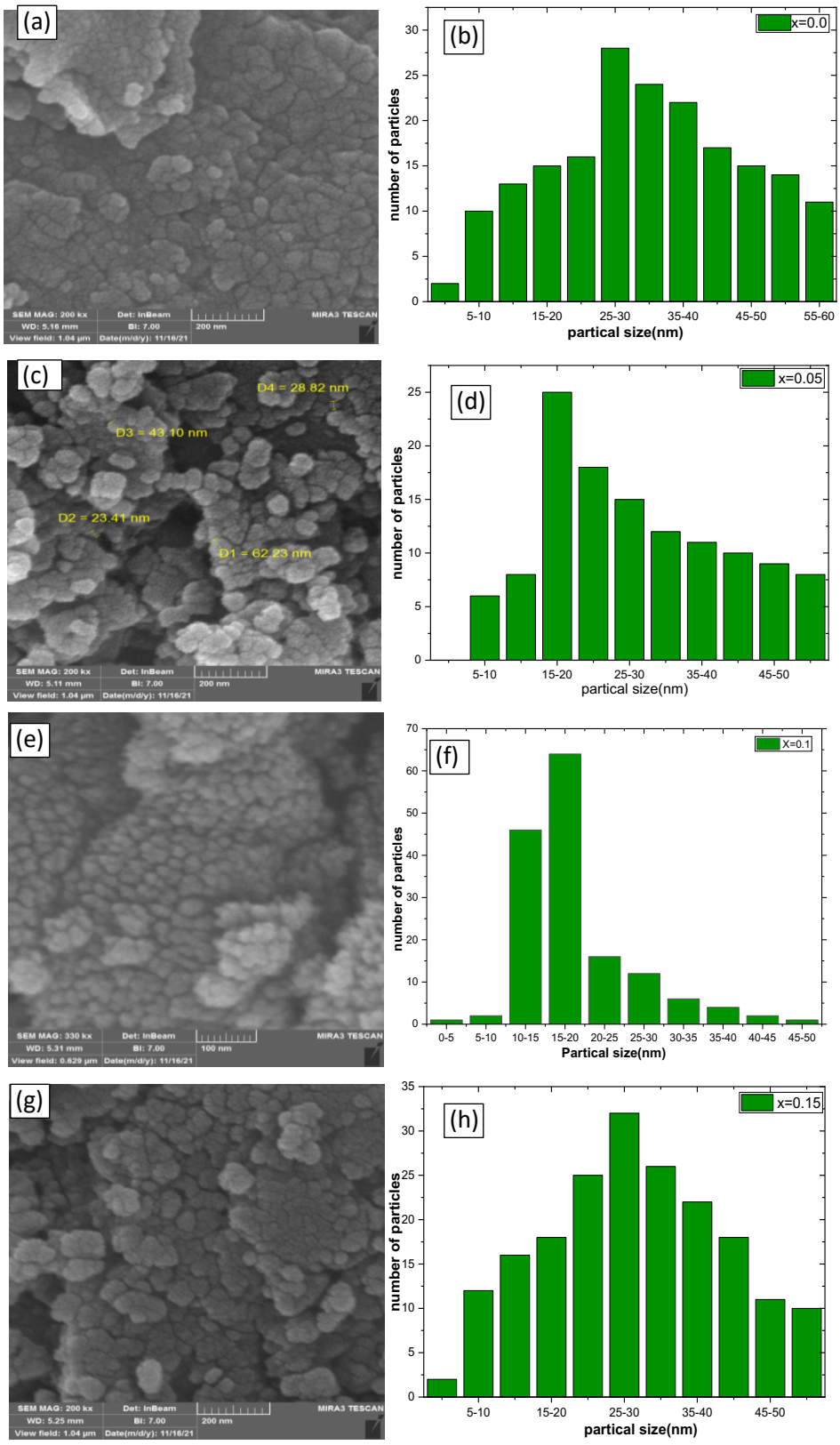

Fig. 3. (a), (c), (e), and (f) are SEM images, and (b), (d), (f), and (h) are their size distributions at x=0, 0.05, 0.1, and 0.15, respectively.

At x=0, the most counted size is ~22.5nm, and the average particle size is about 35nm. At x = 0.05, the most counted size is 17.5nm, while the average is ~25nm. When x = 0.1, the particle size with the most counts is ~15nm, whereas the average is ~20nm. For x = 0.15, the most counted size coincides with the average one, which is 22.5nm. The overall behavior of particle size decreased as x increased to 0.1 and then increased in a similar action to the crystallite size in Table 1. This illustrates the important role of nucleation and growth in controlling particle size. As particle size is larger than crystallite size, each particle has more than one crystal, and the particles are polycrystalline.

3.4. Composition Analysis

Figure 4(a) displays the composition analysis of the sample at x=0.5 obtained by EDX-SEM. The spectrum shows all the used cations besides the oxygen anions. The ratio of Ba/Fe is so close to the ratio in the composition $Ni_{0.5}Ba_{0.5}Fe_2O_4$ that it is proof of the spinel structure's existence.

The washing water was dried and analyzed by EDX-SEM as shown in Figure 4(b). The ratio of Ba/Fe also coincides with the chemical prompt Ni0.5Ba0.5Fe2O4. This analysis is evidence that barium cations did not leave the structure during the auto-combustion process to be soluted cations in the washing water.

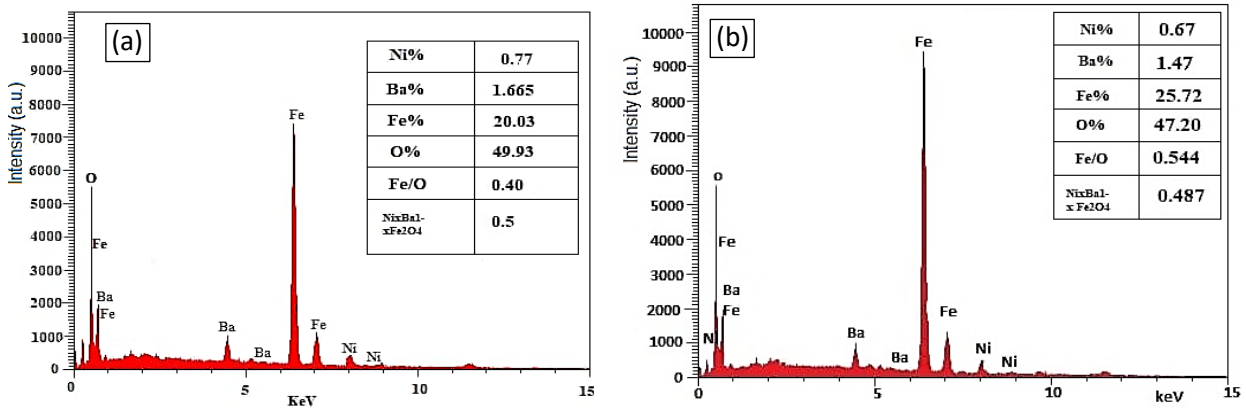

Fig. 4. shows the SEM-EDX spectra of (a) the sample at x = 0.5 and (b) the solid residuals of the washing distilled dried water for the samples at x = 0.5.

3.5. Hysteresis Loop Analysis

Figure 5 shows the measured magnetic hysteresis loops of the $Ni_xBa_{1-x}Fe_2O_4$ samples at x=0, 0.05, 0.1 and 0.15. All samples display an s-shape and soft loop because of the actions of composition and nanosize. Table3 illustrates the Ms of the samples. The degradation of Ms by Ni^{2+} substitution can be explained by the preference of Ni^{2+} ions for octahedral sites (Sadeq, 2019). The redistribution of Fe^{3+} ions from the octahedral sites to tetrahedral sites decreases the magnetic moment (Al-Shakarchi, 2016). As Ni^{2+} ions are magnetic, this replacement will reduce magnetization. The small amount of Ni can produce a large drop in Ms because the octahedral sites are less than tetrahedral ones, besides the reduction in size as in equation (10) (Sadeq, 2017)

$$M_S(D) = M_S(B)\,(1 - 6t/D) \quad \ldots \quad (10)$$

MS(D) is the magnetization for a particle size of D, MS(B) is the magnetization of bulk (70 emu/g) (Singh, 2018), and t is the thickness of the magnetic dead layer.

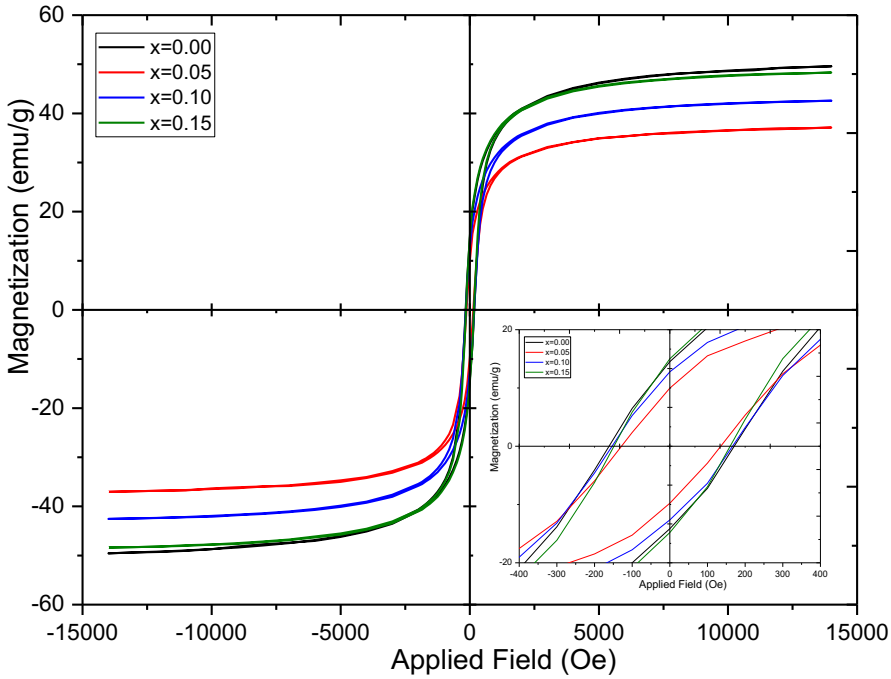

Fig. 5. Hysteresis loops of the prepared $Ni_xBa_{1-x}Fe_2O_4$ at x=0, 0.05, 0.1 and 0.15 with magnification for the loops around the origin.

More Ni^{2+} content will partially position these cations on tetrahedral sites, increasing particle size and Ms. The measured Ms values are comparable to those in (Saba *et al*, 2021; Brightlin, 2016), somewhat lower than in (Eman, 2018), and higher than in (Muhammad *et al*, 2018). The difference is related to particle size, composition, and crystallinity.

The coericivity field Hc variation against (x) is shown in Table 3. Hc depends on particle size for nanomaterial (Sadeq, 2019) besides composition. No clear behavior for this parameter was shown except a minimum value for x=0.05 because of the particle size effect. Comparable values are in (Saba *et al*, 2021; Muhammad *et al*, 2018; Eman, 2018) studies. The measured permeabililty μ follows Ms manner because of the effect of M compared to H. The results of the anisotropy constant Kan were calculated for the samples by the equation (11) (Raghvendra, 2017) and given in Table3, where the variation of Ms is mainly controlling Kan.

$$K_{an} = \frac{M_S H_c}{0.96} \quad \ldots \quad (11)$$

Table 3. The parameters (M_s, M_r, H_c, μ and K_{an}) of the prepared $Ni_xBa_{1-x}Fe_2O_4$ for x=0-0.15.

Sample	Ms (emu/g)	Mr (emu/g)	Hc (Oe)	μ (emu/g.Oe) at 50Oe	K_{an} (emu.Oe/g)
X=0.00	49.686	14.3	168.4	0.347	8715.7
X=0.05	37.142	9.96	132.5	0.254	5126.3
X=0.10	42.536	12.7	161.3	0.260	7146.9
X=0.15	48.267	15.61	154.2	0.359	7752.8

To estimate the particle magnetic moment and Ms, a fitting to the Langevin function was done by Originlab software. The Langevin function for magnetic hysteresis is given in equation (12) (Sadeq, 2020):

$$M(H,T) = M_s\left\{\left[coth\left(\frac{m_p H}{K_B T}\right)\right] - \left(\frac{K_B T}{m_p H}\right)\right\} + \chi_a \, H \quad \ldots \quad (12)$$

$$m_p = \frac{M_s \, \pi \, {D_p}^3}{6} \quad \ldots. \quad (13)$$

Here, m_p, k_B, M(H,T), χ_a and D_p represent the particle magnetic moment, the Boltzmann constant, the magnetization at a temperature T and a field H, the high-field susceptibility and the particle size. The results of the fitting process is given in Table 4. The fitted M_s values in Table 3 are in good agreement with the measured ones given in Table 3 (difference <1%). At a high field, the spinel Ba ferrite susceptibility decreased as Ni content increased due to particle size reduction ([Beji, 2010; Mansour, 2020). The particle magnetic moment according to equation(11) is also given in Table 3, which is nearly a reflection on Ms, as equation (13).

Table 4. Magnetic parameters extracted by Langevin fitting where.

Sample	M_s (emu/g)	$\chi_a \times 10^{-3}$ at 1000 Oe	m_p (μ_B)
x=0.00	50.15	0.55	12133.7
x=0.05	37.41	0.072	3298.6
x=0.10	43.28	0.066	1953.9
x=0.15	49.12	0.026	3157.4

4. Conclusion

The sole-gel auto combustion succeeded in preparing spinel Ba ferrite. The firing process did not modify the crystalline structure clearly, which indicates the composition's thermal stability. The substitution of Ni in Ba ferrite showed different effects on the ferrite properties. The structural property that was affected by substitution is the crystallite size. The FTIR band of the tetrahedral sites seems to be shifted to a higher wave number. The particle distribution and the average particle size are modified by varying the molar ratio. The magnetic properties were altered as substitution was increased, even with a small Ni amount. Ms got a minimum at molar ratio x=0.05 and then increased as x was increased, associated with no dramatic coercivity change. The anisotropy

constant followed Ms. Generally, the prepared spinel Ba ferrite can be effectively modified by adding a small amount of nickel.

References

A. Mulyawan, W. A. Adi, S Mustofa and A. Fisli (2017) The Phase Transformation and Crystal Structure Studies of Strontium Substituted Barium Monoferrite, IOP Conf. Series: Earth and Environmental Science, 58**,** 0120701-10.

Al-Shakarchi, E.K., Lafta, S.H., Musa, A.M. et al. (2016) Effect of Ni Content on Structural and Magnetic Properties of Li-Ni Ferrites Nanostructure Prepared by Hydrothermal Method, Journal of Superconductivity and Novel Magnetism, 29: 923–929.

Badawi M. Ali, Yousef A. Alsabah, Mohamed A. Siddig, Abdelrahman A. Elbadawi, Abdalrawf I. Ahmed, Abdulmajid A. Mirghni, (2020) Influenced of Cu^{2+} Doped on Structural, Morphological and Optical Properties of Zn-Mg-Fe2O4 Ferrite Prepared by Sol-Gel Method, Advances in Nanoparticles, 09(**02**): 10 pages.

B. C. Brightlin, S. Balamurugan (2016) The effect of post annealing treatment on the citrate sol–gel derived nanocrystalline BaFe12O19 powder: structural, morphological, optical and magnetic properties, Applied Nanoscience,6(**8**): 1199-1210.

Bogdan K. Ostafiychuk, Larysa S. Kaykan, Julia S. Kaykan, Bogdan Ya. Deputat and Olena V. Shevchuk (2017) Composition, Microstructure, and Electrical Properties Control of the Powders Synthesized by Sol–Gel Auto-Combustion Method Using Citric Acid as the Fuel, Nanoscale Research Letters,12:1-9.

Ch.Sarda, Ch.Bonino, P.Mollard, A.Rousset (1992) Barium-doped iron oxide pigments for high-density magnetic recording. Thermal stability and magnetic properties, Journal of Magnetism and Magnetic Materials, 109**(1**): 127-132.

Eman S. Al-Hwaitat, Sami H. Mahmood, Mahmoud Al–Hussein, et al. (2018) Structural and Magnetic Properties of Ba3[Cu0.82xZnxMn0.2]2Fe24O41 Z-Type Hexaferrites, Advances in Materials Science and Engineering, 2018, Article ID 6152020, 11 pages.

H. Shokrollahi (2016) The effect of the volume fraction and viscosity on the compression and tension behavior of the cobalt-ferrite magneto-rheological fluids, Elsevier,19: 604–609.

Hanane fodil, mahmoud omari, (2017) structural and physicochemical characterization of barium ferrite nano oxide, International Journal of Advances in Science Engineering and Technology, 2017, 5**(2)**: 50-53.

Khotib, Mohammad, Soegijono, Bambang, Mas'ud, Zainal Alim and Sutriah, Komar (2019) Electrocatalytic Properties of Ni-Doped BaFe12O19 for Oxygen Evolution in Alkaline Solution, Open Chemistry, 17(1):1382-1392.

Mali A, Ataie A (2005) Structural characterization of nanocrystalline BaFe12O19 powders synthesized by sol–gel combustion route, Scripta Materialia, 53, (2005):1065–1070.

Muhammad Shakil Shah, Khuram Ali, Irshad Ali, Asif Mahmood, et al. (2018) Structural and magnetic properties of praseodymium substituted bariumbased spinel ferrites, Elsevier, Materials Research Bulletin , 98:77–82.

Mansour Al-Haj. (2020) Enhanced magnetization in Y substituted Bi0.94Sm0.06FeO3 multiferroic ceramics, Kuwait Journal of Science, 47**(2)**: 34-40.

Raghvendra Singh Yadav, Ivo Kuřitka, Jarmila Vilcakova, Jaromir Havlica, Lukas Kalina, Pavel Urbánek, Michal Machovsky, David Skoda, Milan Masař, Martin Holek (2018) Sonochemical synthesis of Gd3+ doped CoFe2O4 spinel ferrite nanoparticles and its physical properties, Ultrasonics Sonochemistry, 40, Part A: 773-783.

Raghvendra Singh Yadav, Ivo Kuřitka, Jarmila Vilcakova, Jaromir Havlica, et al. (2017) Impact of grain size and structural changes on magnetic, dielectric, electrical, impedance and modulus spectroscopic characteristics of $CoFe_2O_4$ nanoparticles synthesized by honey mediated sol-gel combustion method, Advances in Natural Sciences: Nanoscience and Nanotechnology, 8(**4**): 045002.

Ravleen , Sachin Kumar Godara , Baljinder Kaur , Varinder Kaur and et al. (2020) Characterization of M-type barium hexaferrite synthesized using potatoes as natural fuel, Materials Today: Proceedings, 28, Part 1: 1-3.

Reem S. Khaleel, Mustafa Sh. Hashim, and Samer Gh. Majeed (2022) Synthesis of ZnO thin film by chemical spray pyrolysis using its nano powder, Kuwait Journal of science.49(1):1-11.

Rohit Jasrotiaa, Virender Pratap Singh, Rajesh Kumar, Mahavir Singh (2019) Raman spectra of sol-gel auto-combustion synthesized Mg-Ag-Mn and Ba- Nd-Cd-In ferrite based nanomaterials, Elsevier, Ceramics International, 46:618–621.

Saba Yousaf , Ishtiaq Ahmad , Mudassara Kanwal , Thamraa Alshahrani , Hala H. Alhashim , Nessrin A. Kattan , Hafiz Muhammad Tahir Farid , Ahmer Riaz , Taqi Mehran , A. Laref (2021) Structural and electrical properties of Ba-substituted spinel ferrites, Elsevier, Materials Science in Semiconductor Processing, 122:105488-105495.

Sachin Kumar Godara , Rahul Kumar Dhaka, Navpreet Kaur, Parambir Singh Malhi, Varinder Kaur, Ashwani Kumar Sood, Shalini Bahel, Gopala Ram Bhadu, Jayesh C. Chaudhari, Ishita Pushkarna, Mandeep Singh (2021) Synthesis and characterization of Jamun pulp based M-type barium hexaferrite via sol–gel auto-combustion, Elsevier, Results in Physics, 22:103903-103910.

Sadeq H. Lafta (2017) Effect of pH on Structural, Magnetic and FMR Properties of Hydrothermally Prepared Nano Ni Ferrite, Open Chemistry, 15(**1**) : 53-60.

Sadeq H. Lafta (2020) Evaluation of Hematite Nanoparticles Weak Ferromagnetism, Journal of Superconductivity and Novel Magnetism, 33:3765–3772.

Sadeq H Lafta (2019) Broadband ferromagnetic resonance of non-stoichiometric nano Nickle ferrite with different Ni2+ content, Materials Research Express, 6(**4**):046103.

Sadeq H.Lafta (2017) The Relation of Crystallite Size and Ni2+ Content to Ferromagnetic Resonance Properties of Nano Nickel Ferrites, Journal of Magnetics, 22 **(2**):188-195.

S. Anand, N. Vinnarasi, S. Pauline (2019) Preparation, Characterization and Magnetic Properties of BaZrFe11O19 Nanoparticles via Sol-Gel Auto Combustion Method , Elsevier, Materials Today: Proceedings, 8 Part1: 231–238.

Swati B. Kale, Sandeep B. Somvanshi, M. N. Sarnaik, S. D. More, S. J. Shukla, K. M. Jadhav, (2018) Enhancement in Surface Area and Magnetization of CoFe2O4 Nanoparticles for Targeted Drug Delivery Application, American Institute of Physics, AIP Conference Proceedings, 1953: 030193-1–030193-4.

Tahseen H Mubarak, Lubab Ali Salman, Saib Thiab Alwan, Hussein Sulaiman Mahmood (2017) Preparation of M-type Barium Hexaferrite and Studying Structural and Microwave Properties, Diyala, Journal For Pure Science, 13**(2**):167-182.

T.T. Srinivasan, C. M. Srivastava, N. Venkataramani, and M. J. Patni (1984) Infrared absorption in spinel ferrites, Bull. Mater. Sci., 6**(6**):1063-1067.

V. P. Singh, R. Jasrotia, R. Kumar et al. (2018) A Current Review on the Synthesis and Magnetic Properties of M-Type Hexaferrites Material, World Journal of Condensed Matter Physics,8**(2**): 36-61.

Widyastuti, Nia Sasria, A Marsha Alviani, M Dwi Febri and Vania Mitha (2017) Ni and Zn Substituted M-type Barium Hexaferrite Processed by Sol–Gel Auto Combustion Method, IOP Conf. Series: Journal of Physics: Conf. Series, 877: 012015-012024.

Wei Zhang , Aimin Sun , Xiqian Zhao , Xiaoguang Pan , Yingqiang Han , Nanzhaxi Suo , Lichao Yu , Zhuo Zuo (2019) Structural and magnetic properties of NieCueCo ferrites prepared from sol-gel auto combustion method with different complexing agents, Journal of Alloys and Compounds, 816(**5**):152501-152514.

Yassine Slimani, Munirah Abdullah Almessiere, Sadik Güner, Umran Kurtan and Abdulhadi Baykal (2020) Impacts of Sol-Gel Auto-Combustion and Ultrasonication Approaches on Structural, Magnetic, and Optical Properties of Sm-Tm co-Substituted Sr0.5Ba0.5Fe12O19 Nanohexaferrites: Comparative study, Nanomaterials , 10(**272**):1-18.

Y. K. Dasan, B. H. Guan, M. H. Zahari, L. K. Chuan (2017) Influence of La^{3+} Substitution on Structure, Morphology and Magnetic Properties of Nanocrystalline Ni-Zn Ferrite, PLOS ONE, 12:0170075-0170089.

Yuichi Okazaki, Ikuya Yamada, Shunsuke Yagi (2020) Oxygen Evolution Catalysis for Iron Oxides with Various Structures, MATERIALS TRANSACTIONS, 61(8): 1523-1526.

Yue Liu, a, Yang Li, Ying Liu1, Hong-sheng Yin, Li-li Wang, Kun Sun, Yu Gao (2011) Structure information of barium hexaferrite and strategies for its syntheses, Applied Mechanics and Materials, 69: 6-11.

Zehra Durmus (2014) A Comparative Study on Magnetostructural Properties of Barium Hexaferrite Powders Prepared by Polyethylene Glycol, Hindawi Publishing Corporation, Article ID 302350, 7 pages.

Z. Beji, L. S. Smiri, N. Yaacoub, J.-M. Grenèche, N. Menguy S. Ammar, and F. Fiévet (2010) Annealing Effect on the Magnetic Properties of Polyol-made Ni−Zn Ferrite Nanoparticles Chemistry Materials, 22(**4**):1350–1366.

Submitted: 22/04/2022
Revised: 17/06/2022
Accepted: 18/07/2022
DOI: 10.48129/kjs.20239